WIMP Dark Matter Search Using a 3.1 Tonne-Year Exposure of the XENONnT Experiment

E. Aprile,[1] J. Aalbers,[2] K. Abe,[3] S. Ahmed Maouloud,[4] L. Althueser,[5] B. Andrieu,[4] E. Angelino,[6,7] D. Antón Martin,[8] S. R. Armbruster,[9] F. Arneodo,[10] L. Baudis,[11] M. Bazyk,[12] L. Bellagamba,[13] R. Biondi,[9,14] A. Bismark,[11] K. Boese,[9] A. Brown,[15] G. Bruno,[12] R. Budnik,[14] C. Cai,[16] C. Capelli,[11] J. M. R. Cardoso,[17] A. P. Cimental Chávez,[11] A. P. Colijn,[18] J. Conrad,[19] J. J. Cuenca-García,[11] V. D'Andrea,[7,*] L. C. Daniel Garcia,[4] M. P. Decowski,[18] A. Deisting,[20] C. Di Donato,[21,7] P. Di Gangi,[13] S. Diglio,[12] K. Eitel,[22] S. el Morabit,[18] A. Elykov,[22] A. D. Ferella,[21,7] C. Ferrari,[7] H. Fischer,[15] T. Flehmke,[19] M. Flierman,[18] D. Fuchs,[19] W. Fulgione,[6,7] C. Fuselli,[18] P. Gaemers,[18] R. Gaior,[4] F. Gao,[16] S. Ghosh,[23] R. Giacomobono,[24] F. Girard,[4] R. Glade-Beucke,[15] L. Grandi,[8] J. Grigat,[15] H. Guan,[23] M. Guida,[9] P. Gyorgy,[20] R. Hammann,[9,†] A. Higuera,[25] C. Hils,[20] L. Hoetzsch,[9,11,‡] N. F. Hood,[26] M. Iacovacci,[24] Y. Itow,[27] J. Jakob,[5] F. Joerg,[11] Y. Kaminaga,[3] M. Kara,[22] P. Kavrigin,[14] S. Kazama,[27] P. Kharbanda,[18] M. Kobayashi,[27] D. Koke,[5] K. Kooshkjalali,[20] A. Kopec,[26,§] H. Landsman,[14] R. F. Lang,[23] L. Levinson,[14] I. Li,[25] S. Li,[28] S. Liang,[25] Z. Liang,[28] Y.-T. Lin,[9] S. Lindemann,[15] M. Lindner,[9] K. Liu,[16] M. Liu,[1,16] J. Loizeau,[12] F. Lombardi,[20] J. Long,[8] J. A. M. Lopes,[17,‖] G. M. Lucchetti,[13] T. Luce,[15] Y. Ma,[26] C. Macolino,[21,7] J. Mahlstedt,[19] A. Mancuso,[13] L. Manenti,[10] F. Marignetti,[24] T. Marrodán Undagoitia,[9] K. Martens,[3] J. Masbou,[12] S. Mastroianni,[24] A. Melchiorre,[21,7] J. Merz,[20] M. Messina,[7] A. Michael,[5] K. Miuchi,[29] A. Molinario,[6] S. Moriyama,[3] K. Morå,[1] Y. Mosbacher,[14] M. Murra,[1] J. Müller,[15] K. Ni,[26] U. Oberlack,[20] B. Paetsch,[14] Y. Pan,[4] Q. Pellegrini,[4] R. Peres,[11] C. Peters,[25] J. Pienaar,[8,14] M. Pierre,[18] G. Plante,[1] T. R. Pollmann,[18] L. Principe,[12] J. Qi,[26] J. Qin,[25] D. Ramírez García,[11] M. Rajado,[11] A. Ravindran,[12] A. Razeto,[7] R. Singh,[23] L. Sanchez,[25] J. M. F. dos Santos,[17] I. Sarnoff,[10] G. Sartorelli,[13] J. Schreiner,[9] P. Schulte,[5] H. Schulze Eißing,[5] M. Schumann,[15] L. Scotto Lavina,[4] M. Selvi,[13] F. Semeria,[13] P. Shagin,[20] S. Shi,[1] J. Shi,[16] M. Silva,[17] H. Simgen,[9] A. Stevens,[15] C. Szyszka,[20] A. Takeda,[3] Y. Takeuchi,[29] P.-L. Tan,[19,1] D. Thers,[12] G. Trinchero,[6] C. D. Tunnell,[25] F. Tönnies,[15] K. Valerius,[22] S. Vecchi,[30] S. Vetter,[22] F. I. Villazon Solar,[20] G. Volta,[9] C. Weinheimer,[5] M. Weiss,[14] D. Wenz,[5] C. Wittweg,[11,¶] V. H. S. Wu,[22] Y. Xing,[12] D. Xu,[1] Z. Xu,[1,**] M. Yamashita,[3] J. Yang,[28] L. Yang,[26] J. Ye,[31] L. Yuan,[8] G. Zavattini,[30] Y. Zhao,[16] and M. Zhong[26]

(XENON Collaboration)

[1]*Physics Department, Columbia University, New York, New York 10027, USA*
[2]*Nikhef and The University of Groningen, Van Swinderen Institute, 9747AG Groningen, Netherlands*
[3]*Kamioka Observatory, Institute for Cosmic Ray Research, and Kavli Institute for the Physics and Mathematics of the Universe (WPI), University of Tokyo, Higashi-Mozumi, Kamioka, Hida, Gifu 506-1205, Japan*
[4]*LPNHE, Sorbonne Université, CNRS/IN2P3, 75005 Paris, France*
[5]*Institut für Kernphysik, University of Münster, 48149 Münster, Germany*
[6]*INAF-Astrophysical Observatory of Torino, Department of Physics, University of Torino and INFN-Torino, 10125 Torino, Italy*
[7]*INFN-Laboratori Nazionali del Gran Sasso and Gran Sasso Science Institute, 67100 L'Aquila, Italy*
[8]*Department of Physics, Enrico Fermi Institute and Kavli Institute for Cosmological Physics, University of Chicago, Chicago, Illinois 60637, USA*
[9]*Max-Planck-Institut für Kernphysik, 69117 Heidelberg, Germany*
[10]*New York University Abu Dhabi—Center for Astro, Particle and Planetary Physics, Abu Dhabi, United Arab Emirates*
[11]*Physik-Institut, University of Zürich, 8057 Zürich, Switzerland*
[12]*SUBATECH, IMT Atlantique, CNRS/IN2P3, Nantes Université, Nantes 44307, France*
[13]*Department of Physics and Astronomy, University of Bologna and INFN-Bologna, 40126 Bologna, Italy*
[14]*Department of Particle Physics and Astrophysics, Weizmann Institute of Science, Rehovot 7610001, Israel*
[15]*Physikalisches Institut, Universität Freiburg, 79104 Freiburg, Germany*
[16]*Department of Physics and Center for High Energy Physics, Tsinghua University, Beijing 100084, People's Republic of China*
[17]*LIBPhys, Department of Physics, University of Coimbra, 3004-516 Coimbra, Portugal*
[18]*Nikhef and the University of Amsterdam, Science Park, 1098XG Amsterdam, Netherlands*
[19]*Oskar Klein Centre, Department of Physics, Stockholm University, AlbaNova, Stockholm SE-10691, Sweden*
[20]*Institut für Physik and Exzellenzcluster PRISMA$^+$, Johannes Gutenberg-Universität Mainz, 55099 Mainz, Germany*
[21]*Department of Physics and Chemistry, University of L'Aquila, 67100 L'Aquila, Italy*

[22]Institute for Astroparticle Physics, Karlsruhe Institute of Technology, 76021 Karlsruhe, Germany
[23]Department of Physics and Astronomy, Purdue University, West Lafayette, Indiana 47907, USA
[24]Department of Physics "Ettore Pancini," University of Napoli and INFN-Napoli, 80126 Napoli, Italy
[25]Department of Physics and Astronomy, Rice University, Houston, Texas 77005, USA
[26]Department of Physics, University of California San Diego, La Jolla, California 92093, USA
[27]Kobayashi-Maskawa Institute for the Origin of Particles and the Universe, and Institute for Space-Earth Environmental Research, Nagoya University, Furo-cho, Chikusa-ku, Nagoya, Aichi 464-8602, Japan
[28]Department of Physics, School of Science, Westlake University, Hangzhou 310030, People's Republic of China
[29]Department of Physics, Kobe University, Kobe, Hyogo 657-8501, Japan
[30]INFN-Ferrara and Dipartimento di Fisica e Scienze della Terra, Università di Ferrara, 44122 Ferrara, Italy
[31]School of Science and Engineering, The Chinese University of Hong Kong (Shenzhen), Shenzhen, Guangdong, 518172, People's Republic of China

(Received 25 February 2025; accepted 9 September 2025; published 24 November 2025)

We report on a search for weakly interacting massive particle (WIMP) dark matter (DM) via elastic DM-xenon-nucleus interactions in the XENONnT experiment. We combine datasets from the first and second science campaigns resulting in a total exposure of 3.1 tonne-years. In a blind analysis of nuclear recoil events with energies above 3.8 $\mathrm{keV_{NR}}$, we find no significant excess above background. We set new upper limits on the spin-independent WIMP-nucleon scattering cross section for WIMP masses above 10 GeV/c^2 with a minimum of 1.7×10^{-47} cm^2 at 90% confidence level for a WIMP mass of 30 GeV/c^2. We achieve a best median sensitivity of 1.4×10^{-47} cm^2 for a 41 GeV/c^2 WIMP. Compared to the result from the first XENONnT science dataset, we improve our sensitivity by a factor of up to 1.8.

DOI: 10.1103/msw4-t342

Introduction—Observational evidence from galactic to cosmic scales indicates the existence of massive, non-baryonic dark matter (DM) in the Universe [1]. Among numerous models of DM, weakly interacting massive particles (WIMPs) in the mass range between GeV/c^2 and a few TeV/c^2 are one of the most promising and physics-motivated DM candidates, which are naturally predicted by several extensions of the standard model [2]. Dual-phase liquid xenon (LXe) time projection chambers (TPCs) are currently the most sensitive experiments directly searching for these particles. They have placed stringent upper limits on cross sections for elastic spin-independent (SI) WIMP-nucleon interactions [3–5].

The XENONnT [6] experiment is operated underground at the INFN Laboratori Nazionali del Gran Sasso (LNGS). The experiment consists of three nested detectors: the central LXe TPC housed in a cryostat is enclosed by a neutron veto (NV) detector [7] which is situated within, but optically separated from, a muon veto detector [8]. Both veto detectors are inside a 700-t water tank and function as water Cherenkov detectors. All data used in this Letter were acquired with demineralized water, relying on neutron capture on hydrogen as in [3].

The cylindrical TPC is immersed in 8.5 t of LXe, with gaseous xenon (GXe) on top. Particle interactions in the LXe lead to prompt scintillation light as well as ionization electrons. The light is detected by arrays of photomultiplier tubes (PMTs) at both ends of the cylinder. Electrons are moved toward the liquid surface by an electric drift field, where a stronger extraction field accelerates the electrons into the GXe, leading to a drift-delayed proportional scintillation signal. The measured prompt and delayed light signals are denoted S1 and S2, respectively. The S1–S2 combination allows for energy and three-dimensional position reconstruction. Compared to electronic recoils (ERs), mainly expected from backgrounds, nuclear recoils (NRs) from WIMP scattering feature smaller S2/S1 ratios, allowing for ER/NR discrimination [9].

The sensitive volume of the detector has a diameter of 1.33 m, a maximum electron drift length of 1.49 m, and contains 5.9 t of LXe. All detector construction materials were selected for low radioactivity [10]. The walls are made of polytetrafluoroethylene (PTFE) and cover the inside of the electric field cage [11]. A drift field of 23 V/cm is established between a cathode electrode at the bottom of

*Also at INFN-Roma Tre, 00146 Roma, Italy.
†Contact author: robert.hammann@mpi-hd.mpg.de
‡Contact author: Luisa.Hoetzsch@mpi-hd.mpg.de
§Present address: Department of Physics and Astronomy, Bucknell University, Lewisburg, Pennsylvania, USA.
‖Also at Coimbra Polytechnic—ISEC, 3030-199 Coimbra, Portugal.
¶Contact author: christian.wittweg@physik.uzh.ch
**Contact author: zihao.xu@columbia.edu

the active volume and a gate electrode just below the LXe surface. The extraction field is set between the gate and the anode electrode in the gas phase (2.9 kV/cm in the liquid). All electrodes are composed of parallel wires. Two (four) transverse wires support the gate (anode) wires against sagging. Additional parallel-wire screening electrodes protect the PMT arrays, which contain 494 Hamamatsu R11410-21 3 in. PMTs [12]. PMT pulses above predefined digitization thresholds are recorded with a triggerless data acquisition system [13], stored, and further processed using the software STRAX(EN) [14,15]. Electronegative impurities that affect electron drift and radon emanating from surfaces are continuously removed from xenon via gas + liquid purification and online distillation, respectively [6,16–18]. ^{85}Kr was removed via cryogenic distillation as well at the start of the experiment.

Dataset—In this Letter, 95.1 days of data from the first science run (SR0) of XENONnT, already published in [3], were combined with new data from the second science run (SR1) that lasted from May 19, 2022 to August 8, 2023. The WIMP signal region of the SR1 data was blinded as in [3] until the full analysis procedure had been fixed, while the SR0 data of the previous blind analysis were kept untouched.

During the preparation for SR1, a small amount of xenon with commercial-grade purity was accidentally injected into the system without prior distillation, resulting in increased ER background levels from ^{85}Kr and ^{37}Ar. Rare gas mass spectrometry [19] of xenon samples indicated a molar concentration of a few parts per trillion $^{\mathrm{nat}}$Kr/Xe, which is about a factor 60 higher than the usual level. This initial period of SR1 with an elevated ER background rate is called SR1a and includes one month of cryogenic distillation that reduced the ER background level. The subsequent low-background period is referred to as SR1b. The total live time for SR1 is 186.5 days (66.6 + 119.9 days for SR1a + SR1b). Temperature, pressure, and liquid level remained stable at (177.2 ± 0.4) K, (1.92 ± 0.02) bar, and (4.8 ± 0.2) mm. The liquid level in SR1 was lowered compared to SR0 by 0.2 mm, which mitigated the occurrence of localized bursts of single electron (SE) emission from the top electrodes at high rates, referred to as hot spot. With a 50 V anode voltage increase, the resulting SE gain of (29.4 ± 0.6)PE/e$^-$ (PE denotes photoelectron) was slightly lower than the one in SR0 of 31.2 PE/e$^-$. No changes were made to the drift field. The average "electron lifetime" (defined as the mean time for a drifting electron before being attached to an impurity) in SR1 was $21.8^{+6.7}_{-9.7}$ ms. The PMT performance was monitored with regular LED calibrations, and three additional PMTs (20 in total) were excluded from the SR1 data analysis. In contrast to SR0, the radon distillation system was operated at its full capability in a high-flow LXe + GXe combined mode, which led to an average ^{222}Rn activity concentration of $(0.99 \pm 0.01_{\mathrm{stat}} \pm 0.07_{\mathrm{sys}})$ μBq/kg in SR1a and $(1.10 \pm 0.01_{\mathrm{stat}} \pm 0.09_{\mathrm{sys}})$ μBq/kg in SR1b [with a minimum of $(0.90 \pm 0.01_{\mathrm{stat}} \pm 0.07_{\mathrm{sys}})$ μBq/kg reported in [20]], reducing the associated background from ^{214}Pb ground state β decays by a factor of 1.9 (1.7) in SR1a (SR1b) compared to SR0.

An "event" from a particle interaction is defined by an S1, S2 signal pair. The depth (Z) is reconstructed as the product of electron drift velocity and S1-S2 time difference. The horizontal (X, Y) position is reconstructed from the S2 light distribution on the top PMTs using neural network models [21]. The reconstructed (X, Y, Z) position of the main signal pair is used for signal corrections. The signal reconstruction and corrections in SR1 generally followed the procedures established for SR0 [21]. Since SR0 data are unchanged, we focus on the analysis changes in SR1.

The event position reconstruction in SR1 was improved with an (R,Z)-dependent electron drift velocity from electric field simulations [11]. Additionally, a small charge-insensitive volume located at the outer bottom of the TPC, where electric field lines terminate on the sides of the detector, was included in the correction of the reconstructed (X, Y, Z) positions using uniformly distributed $^{83\mathrm{m}}$Kr events in conjunction with electric field simulations [11].

In SR1, we observed a higher rate of small S2 signals following large signals, attributed to photoionization on impurities in LXe [22]. The delayed electron signals appeared mainly within one full TPC drift time, exhibited a correlation with the preceding signal size, and are time dependent. The light absorption on impurities induced a percent-level time dependence in the absolute S1 signal size, as well as in the S2 signal fraction observed by the PMTs in the bottom array. The time dependence of both observables with respect to their averages over the whole dataset was corrected. We believe this phenomenology is caused by non-electronegative impurities introduced by the change of mode of the radon distillation system, since no correlated change in electron lifetime was observed. In addition, the stability of the detector response was constantly monitored by α decays from ^{222}Rn, and the residual time variation was accounted for in the systematic uncertainties of the S1 and S2 light collection efficiencies.

With the corrected S1 and S2 sizes, denoted as cS1 and cS2, the ER energy in keV$_{\mathrm{ER}}$ is reconstructed as $E = W(\mathrm{cS1}/g_1 + \mathrm{cS2}/g_2)$, with the mean energy needed to produce one observable quantum (photon or electron) of $W = 13.7$ eV [23]. The photon (electron) gains g_1 (g_2), defined as the average number of detected photoelectrons per produced photon (electron), were $g_1 = (0.1367 \pm 0.0010)$ PE/ph and $g_2 = (16.9 \pm 0.5)$ PE/e$^-$.

Data selection criteria were not changed for SR0 and optimized for SR1. A gradient-boosted decision tree (GBDT) was used to reject accidental coincidence (AC)

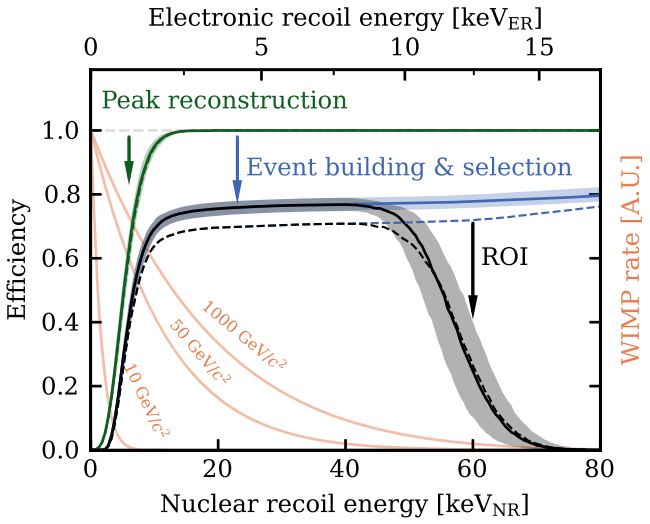

FIG. 1. Efficiencies as functions of NR energy for SR1a (dashed) and SR1b (solid). The peak reconstruction efficiency (green) is determined by the S1 threefold tight coincidence requirement. Adding event building, data selection (blue), and ROI selection (black) lowers the total efficiency. The energy range where it exceeds 10% is [0.6, 13.5] keV$_{NR}$ and $[3.8, 64.1]$ keV$_{NR}$. Recoil energy spectra for three WIMP masses without efficiencies applied are shown in orange. The upper axis shows the conversion of NR energies to the median ER energies.

background from incorrectly paired S1 and S2 signals [24]. This selection was only applied in the "far-wire" region (≥ 4.45 cm from the transverse wires, its complement is termed "near-wire" region), in which the S2 pulse shape is reliably modeled due to lower distortion of the electric field [21]. An S2 threshold of 320 PE was chosen to reduce the risk of AC background mismodeling, higher than the 200 PE in SR0 due to increased AC rates caused by photoionization in SR1. The fiducial volume (FV) retains the same shape as in SR0 but with a tighter radius cut at 58.8 cm, enclosing (4.00 ± 0.15) t of LXe. With respect to the SR0 FV, this tighter radius further excludes 93% of surface background events originating on the detector walls, while retaining 93% of the WIMP signal and leaving the sensitivity nearly unchanged.

The total efficiency consists of signal peak reconstruction, event building, event selection, and region of interest (ROI) selection efficiencies, as shown in Fig. 1. The drop in the peak reconstruction efficiency at low energies arises primarily from the threefold tight coincidence requirement for S1 signals. It is determined via a data-driven approach and validated with Monte Carlo (MC) simulations using WFSim and FUSE [25,26]. The event-building efficiency reflects whether an event will be successfully reconstructed or obscured by, e.g., ambient SE peaks following large S2's, and depends on S1 and S2 signal sizes. It is determined by injecting simulated events, preselected to pass peak reconstruction, at random times into the data and processing them through the analysis pipeline using SALTAX [27] and AXIDENCE [28]. The chance for an event passing the event-building process is anti-correlated with its rejection by selection criteria targeting AC events. Therefore, the efficiency of both processes is evaluated jointly. The event-building efficiency is lower in SR1a than in SR1b due to a higher rate of the hot spot and is evaluated separately for the near- and far-wire regions. Finally, the regions of interest of both SR0 and SR1 are defined as cS1 $\in [0, 100]$ PE and cS2 $\in [10^{2.1}, 10^{4.1}]$ PE. The ROI efficiency uncertainty is primarily determined by the uncertainties in the fitted NR light yield (LY) and charge yield (CY). The total efficiency plateaus at ~71% (77%) for SR1a (SR1b).

Signal and background models—This analysis accounts for backgrounds from ER, NR, AC, and surface events. An internal ^{220}Rn source (external ^{241}AmBe neutron source) is used to constrain the LY and CY of ER (NR). The ER and NR response models are parametrized and fit to the calibration datasets using a Bayesian approach [24] with the software APPLETREE [29], which implements an affine invariant Markov Chain Monte Carlo algorithm [30]. For the ER calibration, approximately 4700 events from the β decay of the Rn daughter ^{212}Pb remained in the ROI after all data selections. In SR0, ^{37}Ar ER calibration was available, enabling a better determination of g_1 and g_2 in the low-energy region, whereas in SR1 it was not. Consequently, a combined ER fit could fail to account for the crucial uncertainty in the ER distribution in cS1, cS2 space, as toy-MC studies have shown that a 1% shift in the ER event distribution along cS2 can lead to a 10% change in sensitivity. To properly capture this uncertainty, we fit ER data separately for SR0 and SR1. For the NR calibration, a clean neutron event sample in the TPC was selected by using the NV to detect the 4.44 MeV γ-ray emitted from the AmBe source in coincidence with the neutron emission with a ~50% probability [31]. This resulted in approximately 5700 neutron events within the ROI. We performed a combined NR fit to both SR0 and SR1 AmBe neutron calibration datasets with shared LY and CY parameters, with an updated parametrization following the NEST v2 model [32]. This allows for a better constraint on the underlying single-scatter NR response from multi-site neutron events, due to the highly spatially localized AmBe events and different source positions in SR0 and SR1. We performed two-dimensional Poisson χ^2 goodness-of-fit (GOF) tests using an equiprobable binning scheme in cS1, cS2 space on each ER and NR best-fit model, which showed no indication of a mismatch between models and data, with the exception of the SR1 NR model with a p-value slightly below the predefined threshold. The impact on the sensitivity of a potential mismodeling in the NR response was found to be small.

The NR response model uncertainties are parametrized as a relative WIMP signal rate uncertainty in the statistical inference. For ER, the number of response model parameters is reduced while retaining realistic model uncertainties to make the WIMP search likelihood computationally

tractable. We use two parameters to represent the ER distribution uncertainty in cS1, cS2 space: one from the principal component decomposition [24] and another from a linear combination of g_1 and g_2 with a correlation coefficient. These two shape parameters are propagated to the statistical inference of the results.

For the SI WIMP model, the energy spectrum is based on the Helm form factor [33] and the standard halo model parameters as suggested in [34].

The dominant background in this analysis is from ER interactions. The contribution from β decays of ^{214}Pb, which constituted the primary ER background in SR0, together with β decays from ^{85}Kr, γ-ray background from detector materials, and solar neutrino-electron scattering, exhibits an approximately flat energy spectrum within the ROI. The double β decays of ^{136}Xe, which have a low expectation in the ROI, are also included in the flat ER component for this Letter. The rate of these ER background components is constrained by a fit to the reconstructed ER energy spectrum in $[20, 140]$ keV$_{\mathrm{ER}}$ outside of the ROI. The best-fit rate is found to be consistent with ancillary measurements of the individual components. For SR1a, the dominant ER background component originates from the elevated level of ^{85}Kr, and a subdominant contribution from the K-shell electron capture of ^{37}Ar (∼2.8 keV). Its rate in SR1a is constrained by extrapolating the ^{37}Ar decay rate from a reference dataset taken before SR1a. While backgrounds from ^{85}Kr and ^{37}Ar were reduced to a subdominant level in SR1b, an additional ER background component, with an energy spectrum resembling β decays of ^{3}H, was present in both SR1a and SR1b. Since this background component only appears in the ROI, its rate was left unconstrained and determined solely from the science data in the ROI, using the ^{3}H spectral shape.

The $LM + LN$ (∼6 keV) and LL (∼10 keV) shell peaks from the double-electron capture (2νECEC) of ^{124}Xe lie within the WIMP search ROI [35]. In [4], the ER background from 2νECEC was fit with a free CY parameter to account for a lower CY due to higher ionization density of electron captures. In our analysis, however, a likelihood-ratio hypothesis test on SR1 data performed after unblinding did not reject the nominal β-yield hypothesis for the $LM + LN$ and LL shell 2νECEC events. Accordingly, we used the nominal model in which 2νECEC is a part of the flat ER component. This strategy was defined before unblinding. Details on the hypothesis test, as well as the results obtained with the alternative model with free 2νECEC CY parameters, are provided in the Supplemental Material [36].

The NR background mainly originates from radiogenic neutrons produced by spontaneous fission and (α, n) reactions in detector materials near the LXe target. A fit to the high-energy γ spectrum suggests that the radioactivity of the inner cryostat flange is significantly higher than expected from material screening results [10]. The neutron expectation from the MC simulations with updated radioactivity is compatible with the data-driven estimate reported in [3]. While the spatial distribution of the neutron background was derived from the updated MC simulations, the rate was estimated from the neutron sideband, defined by multiple-scatter and single-scatter (SS) events tagged by the NV as in [7,24]. The NV tagging efficiency was measured with the same procedure as in [7], resulting in $(55 \pm 2)\%$. With the validated MC framework, the data-driven constraint, and the updated tagging efficiency, the sideband unblinding yields a neutron background expectation in the WIMP ROI of 0.48 ± 0.19 (0.7 ± 0.3) for SR1a (SR1b) and an updated expectation of 0.7 ± 0.3 events for SR0. Another contribution to the NR background is due to coherent elastic

TABLE I. Expectation values of the nominal (prefit) and best-fit models for SR0, SR1a, and SR1b (1.09, 0.73, 1.31 tonne-year, respectively), including an unconstrained WIMP signal with a mass of 200 GeV/c^2. Uncertainties listed in the "nominal" columns correspond to the widths of the Gaussian constraints applied in the likelihood.

	SR0		SR1a		SR1b	
	Nominal	Best fit	Nominal	Best fit	Nominal	Best fit
ER (flat)	134	136 ± 12	430 ± 30	450 ± 20	151 ± 11	154 ± 10
ER (^{3}H-like)			62	40 ± 30	101	80^{+18}_{-17}
ER (^{37}Ar)			58 ± 6	55 ± 5		
Neutron	0.7 ± 0.3	0.6 ± 0.3	0.47 ± 0.19	0.45 ± 0.19	0.7 ± 0.3	0.7 ± 0.3
CEνNS (solar)	0.16 ± 0.05	0.16 ± 0.05	0.010 ± 0.003	0.010 ± 0.003	0.019 ± 0.006	0.019 ± 0.006
CEνNS (atm + DSNB)	0.04 ± 0.02	0.04 ± 0.02	0.024 ± 0.012	0.024 ± 0.012	0.05 ± 0.02	0.05 ± 0.02
AC	4.3 ± 0.9	$4.4^{+0.9}_{-0.8}$	2.12 ± 0.18	2.10 ± 0.18	3.8 ± 0.3	3.8 ± 0.3
Surface	13 ± 3	11 ± 2	0.43 ± 0.05	0.42 ± 0.05	0.77 ± 0.09	0.76 ± 0.09
Total background	152	152 ± 12	553	550 ± 20	257	239 ± 15
WIMP (200 GeV/c^2)		1.8		1.1		2.1
Observed	152		560		245	

neutrino-nucleus scattering (CEνNS) of ^{8}B solar, atmospheric (atm.), and diffuse supernova neutrino background (DSNB). Since neutrinos interact weakly with nuclei, they were modeled as SS events, similar to WIMPs. For all NR components in SR0, the NR response was updated to the best-fit model from the combined SR0 + SR1 calibration fit.

The AC background was modeled in a data-driven approach as in [3,41], using AXIDENCE [28]. The model was validated by the events that satisfy all selection criteria, but fail the GBDT or S2 width requirements [21]. The 154 observed events in the sideband were in agreement with the expectation of 137 events. The uncertainty on the AC background rate in SR1 was calculated as the Poisson uncertainty of the sideband expectation, yielding a relative value of 8.5%.

The surface background in the WIMP ROI originates from β-decay events in the ^{210}Pb decay chain on the surface of the TPC wall. These events can lose a significant fraction of ionization electrons, resulting in comparatively smaller S2 signals. The surface background model was constructed in a data-driven way as in [24]. The radial modeling was improved by using ^{210}Pb events with cS1 $\in [100, 300]$ PE, which better represent the background than the previously used ^{210}Po α events. This update was also applied to SR0. Events outside the FV were used as a sideband to validate the radial distribution of the surface background model, which demonstrated a good match with the data.

Statistical inference—For the statistical analysis of the dataset, we used a log-likelihood-based test statistic with the distributions obtained via toy-MC simulations, as recommended in [34] and detailed in [24]. The computations were performed with the ALEA framework [42]. The likelihood function $\mathcal{L}(\sigma, \boldsymbol{\theta})$ depends on the WIMP-nucleon cross section $\sigma \geq 0$, which is the parameter of interest, and a set of nuisance parameters $\boldsymbol{\theta}$. It factorizes into three components: $\mathcal{L}(\sigma, \boldsymbol{\theta}) = \mathcal{L}_{\text{sci}}(\sigma, \boldsymbol{\theta}) \times \mathcal{L}_{\text{cal}}(\boldsymbol{\theta}) \times \mathcal{L}_{\text{anc}}(\boldsymbol{\theta})$. The science search likelihood function $\mathcal{L}_{\text{sci}}$ itself factorizes into six parts, corresponding to SR0, SR1a, and SR1b, each subdivided into near- and far-wire regions. All six are extended unbinned likelihood functions, which model the data in (cS1, cS2, R) for the far-wire region and in (cS1, cS2) for the near-wire region. $\mathcal{L}_{\text{cal}}$ consists of two unbinned likelihood functions in (cS1, cS2) modeling the ER calibration datasets in SR0 and SR1, and $\mathcal{L}_{\text{anc}}(\boldsymbol{\theta})$ is a product of Gaussian constraints for nuisance parameters from ancillary measurements. The background and signal components are listed in Table I. Apart from the background expectation values, the set of nuisance parameters comprises the WIMP-mass-dependent relative signal efficiency and four ER shape parameters (two for each SR) that modify the shape in (cS1, cS2) of the different ER components. These parameters are tightly constrained by $\mathcal{L}_{\text{cal}}$. The relative signal rate uncertainty is 15% (6%, 4%) in SR0 (SR1a, SR1b) for WIMP masses above ~100 GeV/c^2 and becomes larger for smaller masses. The rate uncertainty in SR1 is smaller than in SR0 due to a smaller selection efficiency uncertainty.

We employed power-constrained limits (PCL) [34,43] to prevent excluding regions of parameter space where our sensitivity is low, which could otherwise occur due to statistical fluctuations or systematic effects. In [3], a conservative power threshold of 0.5 was chosen after identifying an error in the definition of power in [34], effectively truncating the upper limits at the median of the sensitivity band. We have investigated the PCL behavior with toy data, specifically in scenarios involving a shift in the ER event distribution, increased background rates, or increased background uncertainties. These studies revealed no issues that would disqualify a lower power threshold of 0.16. The corresponding truncation of the limits at the -1σ quantile of the sensitivity band allows for a direct comparison with other experiments [4,5].

The SR1 signal region unblinding was performed in two steps. First, events in a small region above the median of the

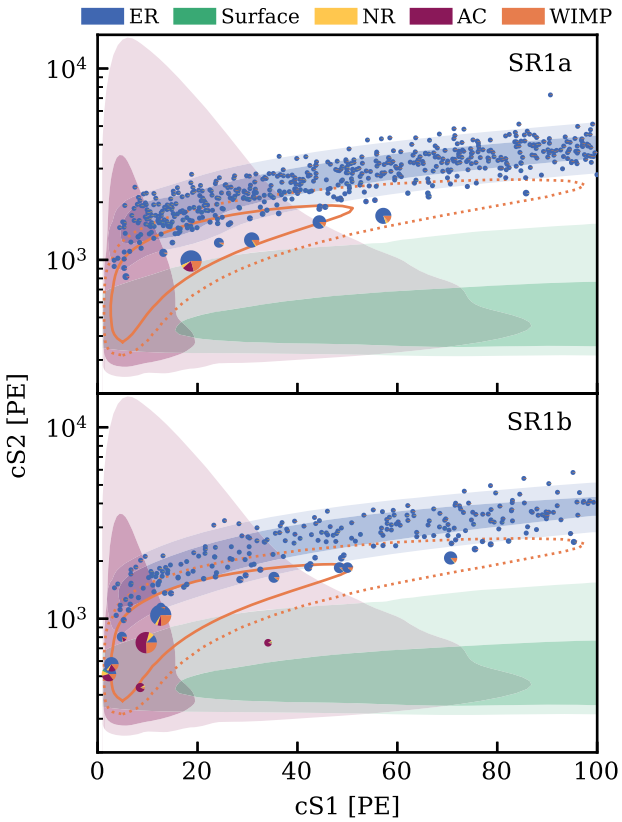

FIG. 2. Distribution of events in cS1, cS2 for SR1a (top) and SR1b (bottom). All data points are represented as pie charts indicating the fraction of the likelihood from the best-fit model including a 200 GeV/c^2 WIMP signal, evaluated at the data point. The scatter size is scaled according to the WIMP likelihood fraction for visualization only. In addition, the one (dark shaded, solid line) and two (light shaded, dotted line) σ contours of the ER, AC, surface background, and 200 GeV/c^2 WIMP signal are shown. The NR background follows a distribution similar to that of WIMPs and is therefore not shown separately.

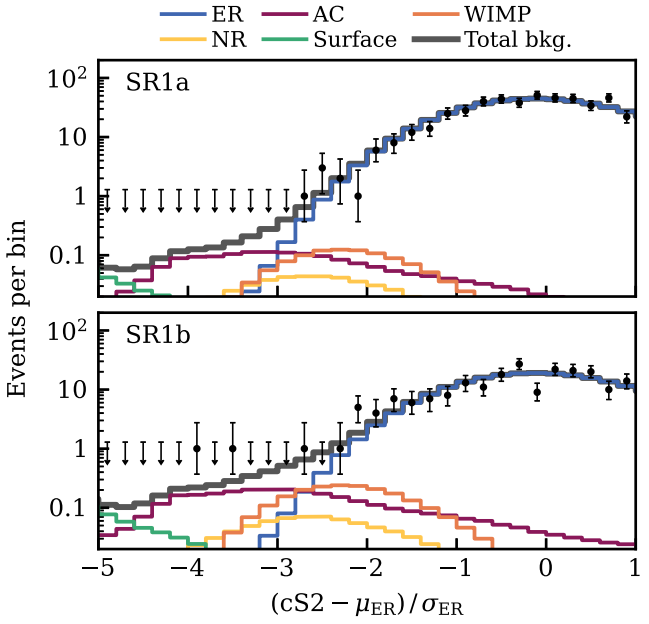

FIG. 3. Distribution in cS2 of the observed data and the best-fit model including an unconstrained 200 GeV/c^2 SI WIMP component in SR1a (top) and SR1b (bottom). The cS2 is normalized by subtracting the median μ_{ER} and dividing by the standard deviation σ_{ER} of the ER distribution along cS1. The gray histogram represents the total background expectation. Black dots represent observed event counts, while triangles mark bins with zero events, both with Poisson confidence intervals.

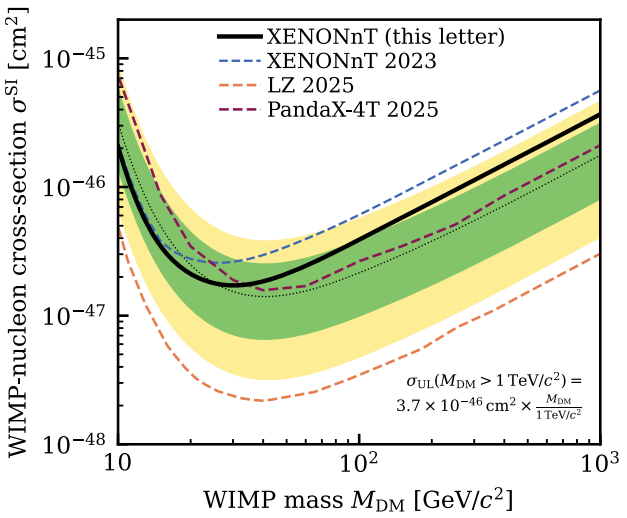

FIG. 4. Upper limits on the SI WIMP-nucleon cross section (90% CL) as a function of the WIMP mass (black line). The sensitivity band is indicated by the region containing 68% (green shaded) and 95% (yellow shaded) of expected upper limits under the background-only hypothesis as well as their median (dotted line). In addition, we show published results from XENONnT using only SR0 data [3], LZ [4], and PandaX-4T [5]. For all, a PCL with a power threshold of 0.16 is used (XENONnT SR0 limit recast accordingly).

NR event distribution with energies above 5 $\mathrm{keV_{ER}}$ were unblinded, containing about 7.5% of expected events from a 1 TeV/c^2 WIMP signal. This initial step allowed us to investigate potential excessive downward leakage of ER events, as previously observed in [3]. The results of the first unblinding step showed no discrepancy with the nominal model. In the second step, all data in the ROI were unblinded. The regions in cS1, cS2 are indicated in Fig. S1 in the Supplemental Material [36].

Results—After unblinding, we observed 560 events in SR1a and 245 in SR1b within the ROI, of which 14 and 13, respectively, lie in the previously blinded region (with two additional events in SR1b, which were already unblinded in [41]). The distribution of all events in (cS1, cS2) is shown in Fig. 2, the corresponding plot for SR0 is Fig. 3 in [3]. Table I shows the best-fit expectation values for all SRs. We performed independent GOF tests on SR1a and SR1b data. The tests were defined before unblinding with p-value thresholds of 2.5% to reject the best-fit model. An unbinned Anderson-Darling (AD) test [44] was performed in the cS2 dimension, after subtracting the cS1-dependent median of the best-fit model. The data and best-fit models in this space are visualized in Fig. 3. Additionally, we performed binned Poisson χ^2 tests using an equiprobable binning scheme in cS1, cS2. We found no indication of mismodeling in any of the tests, with p-values of 0.34 (SR1a) and 0.85 (SR1b) for the AD test and 0.33 (same for SR1a and SR1b) for the Poisson χ^2 test. We also performed an X-Y plane spatial uniformity test of the unblinded events in SR1. It is quantified by the fraction of events in the densest quarter and densest half of the X-Y plane. We found no indication of a spatial asymmetry for SR1.

The local WIMP discovery significance was evaluated for WIMP masses between 10 GeV/c^2 and 1 TeV/c^2. We found no significant excess above backgrounds with the lowest p-value of 0.13 for a WIMP mass of 1 TeV/c^2. We thus report the WIMP-mass-dependent upper limits of the SI WIMP-nucleon cross section at 90% confidence level (CL), shown in Fig. 4 together with the sensitivity band. As we observed no limit below the -1σ sensitivity band, no adjustment is needed to satisfy the power constraint requirement. The most stringent limit on the cross section is 1.7×10^{-47} cm^2 for a WIMP mass of 30 GeV/c^2. For WIMP masses above ~200 GeV/c^2 the limit scales like $M_{\mathrm{WIMP}}/(1\ \mathrm{TeV}/c^2) \times 3.7 \times 10^{-46}$ cm^2. The Supplemental Material [36] includes the limit expressed in terms of the number of WIMP events and the SR1-only result, as well as the limits for spin-dependent WIMP-nucleon coupling.

Summary and outlook—In summary, we have performed a blind analysis of a combined SR0 + SR1 dataset from XENONnT with a total of 186.5 (95.1) days of live time in SR1 (SR0), resulting in a total exposure of 3.1 tonne-year. We found no significant excess above background and placed new limits on the SI WIMP-nucleon interaction

cross section, with an improvement of approximately a factor of 1.5 for WIMP masses above 30 GeV/c^2 compared to the SR0-only results. Running the radon distillation system at its full capacity, we have significantly reduced our ^{222}Rn concentration by a factor 1.9 (1.7) in SR1a (SR1b), resulting in a record-low ER background from ^{214}Pb β decays.

The experiment continues to take data, with an increased NV tagging efficiency due to 0.05% by-weight gadolinium loading, giving an expected factor ∼2 reduction of the neutron background. The recent installation of a charcoal purifier shows promise in removing photoionizing impurities, which is expected to result in a lower AC background rate.

Acknowledgments—We gratefully acknowledge support from the National Science Foundation, Swiss National Science Foundation, German Ministry of Education and Research, Max Planck Gesellschaft, Deutsche Forschungsgemeinschaft, Helmholtz Association, Dutch Research Council (NWO), Fundacao para a Ciencia e Tecnologia, Weizmann Institute of Science, Binational Science Foundation, Région des Pays de la Loire, Knut and Alice Wallenberg Foundation, Kavli Foundation, JSPS Kakenhi, JST FOREST Program, and ERAN in Japan, Tsinghua University Initiative Scientific Research Program, DIM-ACAV+ Région Ile-de-France, and Istituto Nazionale di Fisica Nucleare. This project has received funding and support from the European Union's Horizon 2020 research and innovation program under the Marie Skłodowska-Curie Grant Agreement No. 860881-HIDDeN. We gratefully acknowledge support for providing computing and data-processing resources of the Open Science Pool and the European Grid Initiative, at the following computing centers: the CNRS/IN2P3 (Lyon—France), the Dutch national e-infrastructure with the support of SURF Cooperative, the Nikhef Data-Processing Facility (Amsterdam, Netherlands), the INFN-CNAF (Bologna, Italy), the San Diego Supercomputer Center (San Diego, USA), and the Enrico Fermi Institute (Chicago, USA). We acknowledge the support of the Research Computing Center (RCC) at The University of Chicago for providing computing resources for data analysis. We thank the INFN Laboratori Nazionali del Gran Sasso for hosting and supporting the XENON project.

Data availability—The data that support the findings of this article are openly available [45].

[1] G. Bertone, D. Hooper, and J. Silk, Particle dark matter: Evidence, candidates and constraints, Phys. Rep. **405**, 279 (2005).

[2] L. Roszkowski, E. M. Sessolo, and S. Trojanowski, WIMP dark matter candidates and searches—Current status and future prospects, Rep. Prog. Phys. **81**, 066201 (2018).

[3] E. Aprile *et al.* (XENON Collaboration), First dark matter search with nuclear recoils from the XENONnT experiment, Phys. Rev. Lett. **131**, 041003 (2023).

[4] J. Aalbers, D. S. Akerib, A. K. A. Musalhi, F. Alder, C. S. Amarasinghe, A. Ames *et al.* (LUX-ZEPLIN Collaboration), Dark matter search results from 4.2 tonne-years of exposure of the LUX-ZEPLIN (LZ) experiment, Phys. Rev. Lett. **135**, 011802 (2025).

[5] Z. Bo *et al.* (PandaX Collaboration), Dark matter search results from 1.54 Tonne · Year exposure of PandaX-4T, Phys. Rev. Lett. **134**, 011805 (2025).

[6] E. Aprile *et al.* (XENON Collaboration), The XENONnT dark matter experiment, Eur. Phys. J. C **84**, 784 (2024).

[7] E. Aprile *et al.* (XENON Collaboration), The neutron veto of the XENONnT experiment: Results with demineralized water, Eur. Phys. J. C **85**, 695 (2025).

[8] E. Aprile *et al.* (XENON Collaboration), Conceptual design and simulation of a water Cherenkov muon veto for the XENON1T experiment, J. Instrum. **9**, P11006 (2014).

[9] E. Aprile, C. E. Dahl, L. DeViveiros, R. Gaitskell, K. L. Giboni, J. Kwong, P. Majewski, K. Ni, T. Shutt, and M. Yamashita, Simultaneous measurement of ionization and scintillation from nuclear recoils in liquid xenon as target for a dark matter experiment, Phys. Rev. Lett. **97**, 081302 (2006).

[10] E. Aprile *et al.* (XENON Collaboration), Material radiopurity control in the XENONnT experiment, Eur. Phys. J. C **82**, 599 (2021).

[11] E. Aprile *et al.* (XENON Collaboration), Design and performance of the field cage for the XENONnT experiment, Eur. Phys. J. C **84**, 138 (2024).

[12] A. Antochi *et al.*, Improved quality tests of R11410-21 photomultiplier tubes for the XENONnT experiment, J. Instrum. **16**, P08033 (2021).

[13] E. Aprile *et al.* (XENON Collaboration), The triggerless data acquisition system of the XENONnT experiment, J. Instrum. **18**, P07054 (2023).

[14] J. Aalbers *et al.*, AxFoundation/STRAX: Streaming analysis for xenon experiments (2023), 10.5281/zenodo.1340632.

[15] XENON Collaboration, XENONnT/STRAXEN: Streaming analysis for XENON(nT) (2022), 10.5281/zenodo.5576262.

[16] E. Aprile *et al.* (XENON Collaboration), The liquid-phase xenon purification system of the XENONnT dark matter experiment (to be published).

[17] G. Plante, E. Aprile, J. Howlett, and Y. Zhang, Liquid-phase purification for multi-tonne xenon detectors, Eur. Phys. J. C **82**, 860 (2022).

[18] M. Murra, D. Schulte, C. Huhmann, and C. Weinheimer, Design, construction and commissioning of a high-flow radon removal system for XENONnT, Eur. Phys. J. C **82**, 1104 (2022).

[19] S. Lindemann and H. Simgen, Krypton assay in xenon at the ppq level using a gas chromatographic system and mass spectrometer, Eur. Phys. J. C **74**, 2746 (2014).

[20] E. Aprile *et al.* (XENON Collaboration), Radon removal in XENONnT down to the solar neutrino level, Phys. Rev. X (2025).

[21] E. Aprile *et al.* (XENON Collaboration), XENONnT analysis: Signal reconstruction, calibration, and event selection, Phys. Rev. D **111**, 062006 (2025).

[22] E. Aprile *et al.* (XENON Collaboration), Emission of single and few electrons in XENON1T and limits on light dark matter, Phys. Rev. D **106**, 022001 (2022).
[23] C. E. Dahl, The physics of background discrimination in liquid xenon, and first results from Xenon10 in the hunt for WIMP dark matter, Ph.D. thesis, Princeton University, 2009.
[24] E. Aprile *et al.* (XENON Collaboration), XENONnT WIMP search: Signal and background modeling and statistical inference, Phys. Rev. D **111**, 103040 (2025).
[25] XENON Collaboration, XENONnT/WFSim: V1.0.2 (2022), 10.5281/zenodo.7216324.
[26] XENON Collaboration, XENONnT/FUSE: V1.4.2 (2024), 10.5281/zenodo.16526143.
[27] XENON Collaboration, XENONnT/SALTAX: V0.1.6 (2024), 10.5281/zenodo.17122485.
[28] XENON Collaboration, XENONnT/AXIDENCE: V0.3.2 (2024), 10.5281/zenodo.15459357.
[29] XENON Collaboration, XENONnT/APPLETREE: V0.5.1 (2024), 10.5281/zenodo.14794915.
[30] D. Foreman-Mackey, D. W. Hogg, D. Lang, and J. Goodman, EMCEE: The MCMC hammer, Publ. Astron. Soc. Pac. **125**, 306 (2013).
[31] D. Wenz, Commissioning of the world's first water Cherenkov neutron veto and first WIMP dark matter search results of the XENONnT experiment, Ph.D. thesis, Johannes Gutenberg-Universität Mainz, 2023.
[32] M. Szydagis *et al.*, A review of NEST models for liquid xenon and an exhaustive comparison with other approaches, Front. Detector Sci. Technol. **2**, 1480975 (2025).
[33] R. H. Helm, Inelastic and elastic scattering of 187-MeV electrons from selected even-even nuclei, Phys. Rev. **104**, 1466 (1956).
[34] D. Baxter *et al.*, Recommended conventions for reporting results from direct dark matter searches, Eur. Phys. J. C **81**, 907 (2021).
[35] E. Aprile *et al.* (XENON Collaboration), Double-weak decays of ^{124}Xe and ^{136}Xe in the XENON1T and XENONnT experiments, Phys. Rev. C **106**, 024328 (2022).
[36] See Supplemental Material at http://link.aps.org/supplemental/10.1103/msw4-t342 for detailed discussion about ^{124}Xe double-electron capture, which includes Refs. [37–40].
[37] D. J. Temples, J. McLaughlin, J. Bargemann, D. Baxter, A. Cottle, C. E. Dahl, W. H. Lippincott, A. Monte, and J. Phelan, Measurement of charge and light yields for ^{127}Xe l-shell electron captures in liquid xenon, Phys. Rev. D **104**, 112001 (2021).
[38] P. Klos, J. Menéndez, D. Gazit, and A. Schwenk, Large-scale nuclear structure calculations for spin-dependent WIMP scattering with chiral effective field theory currents, Phys. Rev. D **88**, 083516 (2013); **89**, 029901(E) (2014).
[39] M. Hoferichter, J. Menéndez, and A. Schwenk, Coherent elastic neutrino-nucleus scattering: EFT analysis and nuclear responses, Phys. Rev. D **102**, 074018 (2020).
[40] C. Amole *et al.* (PICO Collaboration), Dark matter search results from the complete exposure of the PICO-60 C_3F_8 bubble chamber, Phys. Rev. D **100**, 022001 (2019).
[41] E. Aprile *et al.* (XENON Collaboration), First indication of solar ^8B neutrinos via coherent elastic neutrino-nucleus scattering with XENONnT, Phys. Rev. Lett. **133**, 191002 (2024).
[42] XENON Collaboration, XENONnT/ALEA: V0.3.0 (2024), 10.5281/zenodo.15724823.
[43] G. Cowan, K. Cranmer, E. Gross, and O. Vitells, Power-constrained limits, arXiv:1105.3166.
[44] T. W. Anderson and D. A. Darling, Asymptotic theory of certain "goodness of fit" criteria based on stochastic processes, Ann. Math. Stat. **23**, 193 (1952).
[45] XENON Collaboration, XENONnT/wimp data release: XENONnT SR0+SR1 results (Version sr0+sr1) (2025), 10.5281/zenodo.17419967.